Nanoscale

Catalytic activity of bimetallic catalysts highly sensitive to the atomic composition and phase structure at the nanoscale†

Shiyao Shan,[a] Valeri Petkov,*[b] Binay Prasai,[b] Jinfang Wu,[a] Pharrah Joseph,[a] Zakiya Skeete,[a] Eunjoo Kim,[a] Derrick Mott,[c] Oana Malis,[d] Jin Luo[a] and Chuan-Jian Zhong*[a]

The ability to determine the atomic arrangement in nanoalloy catalysts and reveal the detailed structural features responsible for the catalytically active sites is essential for understanding the correlation between the atomic structure and catalytic properties, enabling the preparation of efficient nanoalloy catalysts by design. Herein we describe a study of CO oxidation over PdCu nanoalloy catalysts focusing on gaining insights into the correlation between the atomic structures and catalytic activity of nanoalloys. PdCu nanoalloys of different bimetallic compositions are synthesized as a model system and are activated by a controlled thermochemical treatment for assessing their catalytic activity. The results show that the catalytic synergy of Pd and Cu species evolves with both the bimetallic nanoalloy composition and temperature of the thermochemical treatment reaching a maximum at a Pd : Cu ratio close to 50 : 50. The nanoalloys are characterized structurally by *ex situ* and *in situ* synchrotron X-ray diffraction, including atomic pair distribution function analysis. The structural data show that, depending on the bimetallic composition and treatment temperature, PdCu nanoalloys adopt two different structure types. One features a chemically ordered, body centered cubic (B2) type alloy consisting of two interpenetrating simple cubic lattices, each occupied with Pd or Cu species alone, and the other structure type features a chemically disordered, face-centered cubic (fcc) type of alloy wherein Pd and Cu species are intermixed at random. The catalytic activity for CO oxidation is strongly influenced by the structural features. In particular, it is revealed that the prevalence of chemical disorder in nanoalloys with a Pd : Cu ratio close to 50 : 50 makes them superior catalysts for CO oxidation in comparison with the same nanoalloys of other bimetallic compositions. However, the catalytic synergy can be diminished if the $Pd_{50}Cu_{50}$ nanoalloys undergo phase segregation into distinct chemically-ordered (B2-type) and disordered (fcc-type) domains. This finding is significant since it provides a rational basis for streamlining the design and preparation of Pd-based nanoalloy catalysts in terms of atomic structure and phase state.

1. Introduction

Recently the interest in alloying of palladium (Pd) with transition metals on the nanoscale has surged in comparison with the extensive studies of platinum (Pt)–transition metal nanoalloys. The surge is due to the fact that Pd offers opportunities

[a]*Department of Chemistry, State University of New York at Binghamton, Binghamton, NY 13902, USA. E-mail: cjzhong@binghamton.edu*
[b]*Department of Physics, Central Michigan University, Mt. Pleasant, Michigan 48859, USA. E-mail: petko1vg@cmich.edu*
[c]*School of Materials Science, Japan Advanced Institute of Science and Technology, 1-1 Asahidai, Nomi, 923-1292 Ishikawa, Japan*
[d]*Department of Physics, Purdue University, West Lafayette, IN, USA*
†Electronic supplementary information (ESI) available: Additional HE-XRD/ PDFs, XPS, and other experimental data. See DOI: 10.1039/c5nr04535e

for preparation of low-cost, highly-active and stable catalysts.[1–21] For example, Pd–nickel (Ni) nanoalloys are being explored as catalysts for catalytic reactions such as oxygen reduction, alcohol oxidation, methane combustion, and hydrogenation reactions,[4–24] which are very important for energy sustainability. Among the different Pd-based alloys, there has been increasing interest in the nanoalloys of Pd and copper (Cu), partly triggered by recent theoretical studies. For example, a recent theoretical study on the catalytic activity of PdCu alloys for the oxygen reduction reaction (ORR)[25] predicted that Cu would reduce Pd–O binding energy whereas Pd would increase Cu–O binding energy due to charge transfer from Cu to Pd. It also predicted that the increased overlap between the d-states of Pd and the adsorbed oxygen species would make the reduction of oxygen binding energy at Pd sites

more significant than the increase of oxygen binding energy at Cu sites. As such, the activity of Pd–Cu nanoalloys for ORR would peak at a Pd : Cu ratio of 50 : 50. Furthermore, studies of the so-called lattice strain effect on the reactivity of Pd–Cu alloys with a Pd-rich surface[26] indicated that the strength of adsorption of OH_{ads} and O_{ads} species and the magnitude of strain in Pd–Cu alloys are strongly correlated. In an early theoretical study of PdCu bulk and surface alloys,[27] CO adsorption energy was found to be significantly improved for Cu-rich Pd–Cu nanoalloys, due to a downshift of the d band center of Pd. DFT studies on various slabs (*e.g.* fcc, bcc, hcp) of PdCu alloys predicted that an L1-fcc type slab made of Pd and Cu layers packed along the [111] direction of an fcc cell would exhibit a significant enhancement of the catalytic activity for ORR reaction. Notably, the study predicted a synergistic effect of mixing Pd and Cu in a ratio of 50 : 50.[28] DFT calculation also predicted a strong electronic effect in PdCu alloys causing a shift of CO adsorption sites from three-fold hollow sites to bridge Pd sites. The effect would take place when Cu atoms are selectively inserted into the Pd (111) surface, leading to a less perturbation of the electronic structure of the nearby Pd sites.[29] The result implies that the arrangement of Cu species with respect to Pd species could lead to an atomic ensemble effect, influencing strongly the catalytic activity.

Several experimental studies of PdCu alloys have demonstrated the importance of tuning the atomic structure and morphology of the nanoalloys for achieving better catalytic properties. Examples include porous Pd–Cu nanoalloys,[17] composition-tuned Pd–Cu nanoalloys,[18,19] and Pt-shell–PdCu-core type nanoalloys.[8] In a study on CO and NO elimination over PdCu nanoalloy catalysts, the catalytic properties were found to be tunable by taking advantage of metal–active support interface interactions.[30] Another early study on CO oxidation over PdCu single crystal alloys with a Pd-rich surface demonstrated an increase of the surface Cu : Pd ratio from 0.1 to 0.7 due to diffusion of Cu from the bulk to the surface of the Pd–Cu crystal.[31] PdCu nanoalloys on active Al_2O_3 and TiO_2 supports have been shown to exhibit high activity for CO removal under an ambient atmosphere.[32] $Cu_2Cl(OH)_3$ species have also been found to improve the catalytic activity of Pd–Cu nanoalloys by promoting the re-oxidation of Pd(0) to Pd(2+) species.[32] A recent study on the hydrogen storage properties of the surface of PdCu thin films has revealed that the solubility of hydrogen is much lower when the film possesses a body-centered-cubic (bcc) as compared to the case with a face-centered-type (fcc) structure.[33] In addition to gas-phase reactions, there have also been studies focusing on understanding dealloying of Pt/Pd–transition metal alloy catalysts in fuel cells in terms of the formation of the so-called Pt/Pd skin.[6,8,17,34] The nanoporous PdCu alloys formed by dealloying of PdCuAl alloy nanoparticles in an alkaline solution would significantly enhance the stability and activity of PdCu-based catalysts used in fuel cells.[17] A nanoporous PdCu core capped with a Pt shell was also shown to exhibit a synergetic effect in electrocatalysis.[8,35]

Despite numerous experimental and theoretical studies,[36,37] the question of how exactly the catalytic activity of PdCu nanoalloys is influenced by their bimetallic composition and atomic-scale structure remains rather elusive. Recently we studied PdNi nanoalloys to reveal how Pd and Ni atoms are arranged across alloy particles, including particle's surface, and how this arrangement contributes synergistically to improving the catalytic activity of the alloys for CO oxidation reaction.[38,39] We found that the contribution arises from a unique combination of the first atomic neighbor distances and coordination numbers for Pd and Ni atoms at particle's surface.[38,39] Here we report new findings of the study of PdCu nanoalloys, aiming at understanding the correlation between the atomic-scale structure and the catalytic activity for CO oxidation. This understanding is aided by both *ex situ* and *in situ* synchrotron X-ray diffraction (XRD), including atomic pair distribution function (PDF) analysis.

2.   Experimental section

2.1   Chemicals

Palladium(II) acetylacetonate (Pd(acac)₂, 97%), palladium(II) acetate (Pd(OCOCH₃)₂, 98%), potassium tetrachloropalladate (K₂PdCl₄), copper(II) acetylacetonate (Cu(acac)₂, 97%), benzyl ether ((C₆H₅CH₂)₂O, >98%), oleylamine (CH₃(CH₂)₇CH CH(CH₂)₈NH₂, 70%), 1,2-hexadecanediol (90%), ethylene glycol anhydrous (99.8%) and oleic acid (CH₃(CH₂)₇CH=CH-(CH₂)₇COOH, 99+%) were purchased from Aldrich. Other chemicals such as ethanol, hexane, copper chloride and potassium chloride were purchased from Fisher Scientific. Vulcan carbon XC-72 was from Cabot. Pd (20% on activated carbon (Pearlman's catalyst), unreduced, 50% water wet paste (Escat™ 1951, BASF kit)) was obtained from Strem Chemicals. Gases of CO (1 vol% balanced by N₂), H₂ (15 vol% balanced by N₂) and O₂ (20 vol% balanced by N₂) were purchased from Airgas. All chemicals were used as received.

2.2   Synthesis of PdCu nanoalloys and preparation of catalysts

Pd$_n$Cu$_{100-n}$ alloy nanoparticles (NPs) (n represents the atomic percentage of Pd in the NPs) were synthesized using two different methods.[18,21] One method involved using benzyl ether (B-) as a solvent to produce PdCu alloy NPs of different compositions[21] (noted as (B-) PdCu), and the other method used ethylene glycol (E-) as a solvent to produce PdCu alloy NPs of different compositions[18] (noted as (E-) PdCu). Briefly, for (B-) PdCu NPs, palladium(II) acetylacetonate and copper(II) acetylacetonate in a controlled molar ratio were dissolved into benzyl ether solvent. 1,2-Hexadecanediol was added as a reducing agent. Temperature was increased slowly to 105 °C until the metal precursors started to decompose and the solution turned dark, at which point oleic acid and oleylamine were added as capping agents under a N₂ atmosphere. The mixture was heated up to 220 °C with reflux for 0.5 h and then cooled down to room temperature. NPs were precipitated out by adding ethanol and centrifuging, and then dispersed in hexane solvent for further use. (E-) PdCu NPs were synthesized similarly except using palladium acetate as the precursor and

ethylene glycol as both the solvent and reducing agent.[18] Palladium and copper nanoparticles were also synthesized differently using two phase methods reported previously.[21,40]

2.3 Catalyst preparation

Active catalysts were prepared from the as-synthesized PdCu alloy NPs as follows. First, the alloy NPs were deposited on carbon powder (XC-72) by adding a controlled amount of the as-synthesized NPs to the suspension of XC-72 carbon powder in hexane, followed by sonication and overnight stirring. The resulting carbon supported NPs were then collected by removing the solvent and dried under N_2. Second, carbon supported NPs were activated by a controlled thermochemical treatment.[41,42] In brief, the treatment involved treating of carbon supported NPs at 260 °C under an O_2 or N_2 atmosphere for 1 h to remove the organic capping molecules, and further treating at 400 °C under a 15% H_2–85% N_2 atmosphere for 2 h for calcination in a programmable furnace. The catalysts, termed fresh catalysts, were loaded in a custom-built thermally-controlled reactor for further thermochemical treatment and catalytic activity testing. Commercial carbon supported Pd NPs (Pd/C) were treated at 400 °C under 15% H_2 balanced by N_2 for 1 h, yielding a loading of 20 wt% Pd NPs on the carbon support. For most carbon supported PdCu nanoalloy catalysts (PdCu/C), the NP weight loading on the carbon support was close to 20% (15% for $Pd_{21}Cu_{79}$/C, 23% for $Pd_{48}Cu_{52}$/C, and 15% for $Pd_{75}Cu_{25}$/C) as determined by thermogravimetric analysis (TGA) performed on a Perkin-Elmer Pyris 1-TGA instrument. TEM analysis showed that the sizes of (B-) Pd_nCu_{100-n} alloy NPs were 5.7 ± 0.5, 5.5 ± 0.5, and 5.5 ± 0.8 nm for n = 21, 54, and 75, respectively. NPs of other compositions were also synthesized, which showed similar particle sizes (e.g., (B-) $Pd_{48}Cu_{52}$ showed a size of about 5.8 nm). The as-synthesized (E-) $Pd_{21}Cu_{79}$, $Pd_{58}Cu_{42}$ and $Pd_{77}Cu_{23}$ NPs appeared to be 2.7 ± 0.5, 2.6 ± 0.6 and 3.5 ± 0.7 nm in size, respectively. The size of the commercial Pd/C NPs was found to be around 7 nm.

2.4 Catalytic activity measurement

The catalytic activity of PdCu nanoalloy catalysts for catalytic CO oxidation reaction carried out under a (0.5 vol% CO + 10 vol% O_2 balanced by N_2) atmosphere was measured using a customer-built system including a temperature-controlled reactor, gas flow/mixing/injection controllers, and an on-line gas chromatograph (Shimadzu GC 8A) equipped with 5A molecular sieves, Porapak Q packed columns and a thermal conductivity detector. The activated nanoalloys were loaded in the middle of a quartz micro-reactor tube (inner diameter: 4 mm) and wrapped by quartz wool forming a "catalyst bed" with a length of 6 mm. The feeding gas (0.5 vol% CO + 10 vol% O_2 balanced by N_2) was injected continuously through the fixed catalyst bed in the quartz micro-reactor at a flow rate of 20 mL min^{-1}. The residence time was about 0.2 seconds. The gas hourly space velocity (GHSV) in the system was around 16 000 h^{-1}. Temperature control was achieved by using a furnace coupled with a temperature controller. The catalytic activity for CO oxidation was determined by analyzing the tail gas effusing from the quartz micro reactor using an on-line gas chromatograph.

2.5 Characterization of the morphology, chemical composition and ordering pattern

High-angle annular dark-field scanning TEM (HAADF-STEM) was used to characterize the morphology of the Pd–Cu alloy NPs. Energy dispersive X-ray spectroscopy (EDS) was used to obtain elemental mapping and determine the chemical species pattern of the PdCu alloy NPs. Experiments were carried out on a JEOL JEM 2010F with an acceleration voltage of 200 kV and a routine point-to-point resolution of 0.194 nm. TEM analysis was performed using an FEI Tecnai T12 Spirit Twin TEM/SEM electron microscope (120 kV). The nanoparticle samples were suspended in hexane solution and were dropcast onto a carbon-coated copper grid followed by solvent evaporation in air at room temperature.

Inductively Coupled Plasma-Optical Emission Spectroscopy (ICP-OES) was used to determine the overall chemical composition of the PdCu NPs. Measurements were performed on a Perkin Elmer 2000 DV ICP-OES instrument utilizing a Meinhardt nebulizer coupled to a cyclonic spray chamber to increase analyte sensitivity with the following parameters: 18.0 L $Ar_{(g)}$ min^{-1}; auxiliary 0.3 L $Ar_{(g)}$ min^{-1}; nebulizer 0.63 L $Ar_{(g)}min^{-1}$; power 1500 W; peristaltic pump rate 1.00 mL min^{-1}. Laboratory check standards were analyzed for every 6 or 12 samples and the instrument was re-calibrated if the check standards were not within ±5% of the initial concentration.

X-ray photoelectron spectroscopy (XPS) measurements were performed ex situ using a Physical Electronics Quantum 2000 scanning ESCA microprobe. This instrument was equipped with a focused monochromatic Al Kα X-ray (1486.7 eV) source for excitation, a spherical section analyzer and a 16-element multichannel detection system. The X-ray beam was approximately 100 μm in diameter. It was rastered over a 1.4 mm by 0.2 mm rectangle spot on the sample. During rastering the incident X-ray beam was normal to the sample while the X-ray detector tilted at 45° away from the normal. The binding energy (BE) of the chemical species adsorbed at the NP surface was calibrated using the C 1s peak at 284.8 eV as an internal standard. The percentages of the individual elements detected were determined by analyzing the areas of the respective peaks.

2.6 In situ and ex situ synchrotron high energy X-ray diffraction (HE-XRD) experiments and atomic pair distribution function (PDF) derivation

Synchrotron XRD experiments were carried out at Sector 11 of the Advanced Photon Source both in ex situ and in situ modes using X-rays with a wavelength, λ, of 0.1080 Å (X-ray energy ~115 keV) and 0.1378 Å (X-ray energy of ~95 keV), respectively. For the ex situ experiments carbon supported nanoalloy catalyst samples were loaded into thin-wall glass capillaries with a diameter of 1.5 mm and XRD data were collected at room temperature under an ambient atmosphere. For the in situ experiments the catalyst samples were loaded into quartz tubes with a diameter of 1 mm and wrapped with quartz wool.

The tubes were inserted into a gas flow reactor-type cell allowing for collecting XRD data under a controlled gas atmosphere and temperature.[43]

Experimental XRD data were corrected for experimental artifacts, reduced to the so-called structure factors, $S(q)$, and then Fourier transformed to atomic PDFs $G(r)$, using the relationship:

$$G(r) = \frac{2}{\pi} \int_{q=0}^{q_{max}} q[S(q) - 1] \sin(qr) dq \qquad (1)$$

here q is the wave vector defined as $q = 4\pi \sin(\theta)/\lambda$, where θ is half of the scattering (Bragg) angle and λ is the wavelength of X-rays used. In the present experiments XRD data were collected up to wave vectors q_{max} of 25 Å^{-1}. Note, as derived, atomic PDFs $G(r)$ are experimental quantities that oscillate around zero and show positive peaks at real space distances, r, where the local atomic density $\rho(r)$ exceeds the average one ρ_o. This behavior can be expressed by the equation $G(r) = 4\pi r \rho_o[\rho(r)/\rho_o - 1]$, which is the formal definition of the PDF $G(r)$. HE-XRD and atomic PDFs have already been proven to be very efficient in studying the atomic-scale structure of nanometer-sized materials, including metallic NPs.[44,45]

In addition, *in situ* real-time X-ray diffraction was performed at the beamline X20C at the National Synchrotron Light Source at Brookhaven National Laboratory. The energy of the X-rays is 6.9 keV (λ =1.79 Å).[40]

3. Results and discussion

In this section, experimental data from the *ex situ* and *in situ* HE-XRD/atomic PDF analysis will be discussed first in terms of the catalyst phase state and structure type as a function of bimetallic composition of nanoalloys. Then the experimental data for the catalytic activity of PdCu nanoalloy catalysts for CO oxidation are correlated with the data for the atomic structure. The correlations are used as a basis for rationalizing the bimetallic composition–atomic structure–catalytic activity relationships in PdCu nanoalloy catalysts.

3.1 Morphology and composition

To determine the controllability of the synthesis protocol with respect to the bimetallic composition, the composition of the as-synthesized (B-) Pd_nCu_{100-n} nanoparticles was analyzed by ICP-OES. Fig. 1A shows a representative plot of n in Pd_nCu_{100-n} NPs as determined by ICP-OES *vs.* the nominal feeding in terms of the atomic fraction m (*i.e.*, mPd and $(100-m)$Cu) in the NP synthesis. The plot shows that the relative amount of Pd in the PdCu NPs increases approximately linearly with the feeding Pd% in the synthesis solution. This finding indicates that the bimetallic composition of the as-synthesized PdCu NPs can be well controlled by the relative concentration of Pd in the synthesis solution, *i.e.*, by the feeding composition used in the synthesis protocol.

The size of the as-synthesized (B-) Pd_nCu_{100-n} NPs are 5.7 ± 0.5, 5.5 ± 0.5, and 5.5 ± 0.8 nm for n = 21, 54, and 75, respectively, whereas the sizes of the thermochemically-treated carbon supported Pd_nCu_{100-n} are 7.4 ± 1.2, 6.0 ± 0.8, and 4.9 ± 0.5 nm respectively. The particles appear spherical in shape and uniformly distributed over the carbon support. The size, shape and distribution of Pd and Cu species across the treated NPs, *i.e.*, the chemical pattern, were further analyzed by HAADF-STEM and EDS mapping analysis. A representative set of results is shown in Fig. 1B. The HAADF-STEM images show that the thermochemically-treated PdCu NPs are largely crystalline. Elemental mapping and EELS scans show that Pd and Cu species are uniformly distributed across the NPs, confirming their alloy-type character (Fig. 1B). Note that the bimetallic
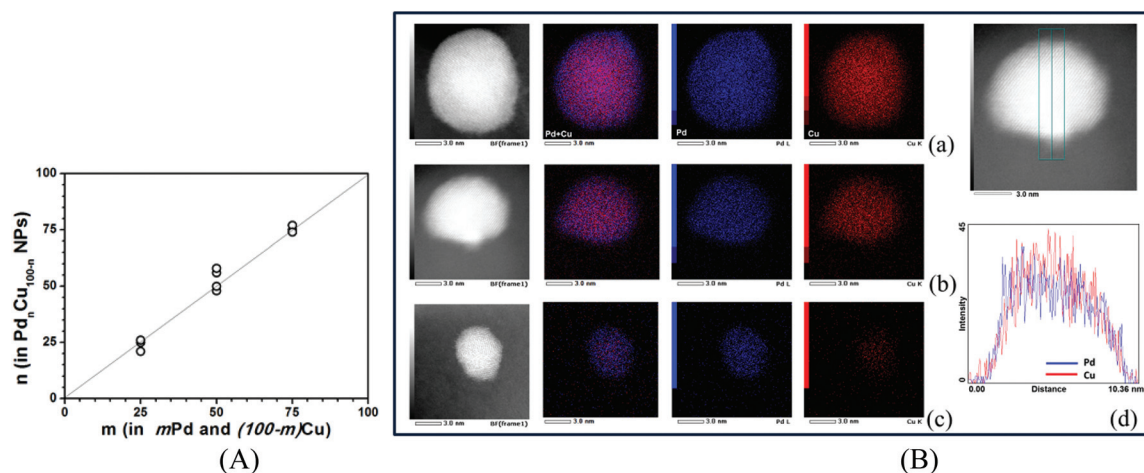

Fig. 1 (A) Plot of Pd% (n) in the as-synthesized Pd_nCu_{100-n} NPs, as determined by ICP, against the synthesis feeding ratio expressed as (m) Pd and $(100 - m)$ Cu and (B) high-angle annular dark field scanning TEM (HAADF-STEM) images: morphological imaging and elemental mapping for (a) $Pd_{21}Cu_{79}$, (b) $Pd_{48}Cu_{52}$, (c) $Pd_{75}Cu_{25}$ nanoparticles and the corresponding EELS line scans of the single $Pd_{48}Cu_{52}$ nanoparticle shown in (d) for Pd (blue) and Cu (red).

composition of the alloy NPs determined by EDS is consistent with that determined by ICP, confirming the Pd : Cu ratios. In comparison with (B-) PdCu NPs, the as-synthesized (E-) PdCu NPs (Fig. S1†) appeared somewhat smaller, showing 2.7 ± 0.5, 2.6 ± 0.6 and 3.5 ± 0.7 nm in diameter, respectively, for (E-) $Pd_{25}Cu_{75}$, $Pd_{58}Cu_{42}$ and $Pd_{77}Cu_{23}$ NPs.

To reveal the speciation and relative surface distribution of Pd and Cu species for the (B-) PdCu NPs, surface-sensitive XPS analysis was carried out (Fig. S2†). The binding energies (in eV) determined for Pd and Cu species are summarized in Table S1.† The data show that the surface and bulk chemical compositions of Pd–Cu alloy NPs are rather similar, proving that (i) NPs are nanoalloys, and (ii) the chemical composition of NPs does not change significantly close to/at the NP surface. Note, the binding energy of Pd species for PdCu NPs appears to vary with the bimetallic composition, showing a minimum for Pd : Cu ratio at ~50 : 50. The binding energy of Cu species appears to change significantly with the bimetallic composition. In particular, the data suggest a possible presence of Cu(+2/+1) species in $Pd_{21}Cu_{79}$/C and $Pd_{48}Cu_{52}$/C, and mostly Cu(0) species in $Pd_{75}Cu_{25}$/C. The partial oxidation of Cu in PdCu alloy NPs with Pd : Cu ratio <50 : 50 is very likely due to air exposure before XPS analysis.

3.2 In situ XRD characterization of thermal evolution of mixed Pd and Cu nanoparticles

In order to understand the evolution of the phase state of PdCu alloy NPs in real time,[40] an *in situ* synchrotron XRD study was performed for revealing the formation of Pd–Cu nanoalloys from a mixture of Pd and Cu NPs dispersed on carbon black and then supported on Si wafer. Measurements were performed under a He atmosphere at 300 °C and then a H_2 atmosphere heated up to a temperature of 700 °C. A representative set of XRD patterns is shown in Fig. 2. The patterns indicate that Pd and Cu NPs alloyed into a chemically ordered bcc (B2-type) phase after being heated up to 300 °C. Upon

further heating to 450 °C the alloy appears to undergo a transformation to a chemically disordered state that is of the fcc-type structure (see Fig. 2A and B). The arrow shown in Fig. 2B indicates the critical temperature for the phase transformation. The lattice parameter of the chemically ordered (bcc; B2-type) phase was estimated to be 2.93 ± 0.01 Å. The chemically disordered fcc-type alloy phase exhibited peaks at 50.2° (111) and 58.2° (200), indicating a fcc lattice parameter of 3.68 Å. The non-symmetric shape of the (111) peak, however, indicates that the transformation is incomplete, even at 700 °C. From the peak's full width at half maximum, the size of atomic domains scattering X-rays coherently was estimated to be *ca.* 6 nm. Note that no significant NP growth was observed up to the highest temperature used in the measurement.

Based on the results from the real-time *in situ* study, it may be concluded that Pd and Cu NP species, when they are mixed and heated up to 300 °C under an inert (He) atmosphere under the measurement conditions, tend to form a chemically ordered (bcc, B2-type) phase at first. Further heating up to 450 °C triggers a gradual transition into a chemically disordered (fcc-type) alloy phase. Both chemically disordered and ordered PdCu nanoalloy phases coexist over a broad temperature range up to 700 °C. For the PdCu nanoalloys synthesized and thermochemically treated in this work, a more detailed picture of the phase states was obtained by *ex situ* and *in situ* HE-XRD/atomic PDF studies described below.

3.3 Ex situ and in situ HE-XRD/PDF structure studies on Pd_nCu_{100-n} nanoalloys

(A) Ex situ study. Experimental HE-XRD patterns and the respective atomic PDFs for a set of carbon supported (B-) Pd_nCu_{100-n} NPs treated under O_2 at 260 °C for 1 h and then under H_2 at 400 °C for 2 h are shown in Fig. 3A and 3B, respectively.

Analysis of the data in Fig. 3 reveals a rather unusual pattern. In particular, when one of the two metallic species
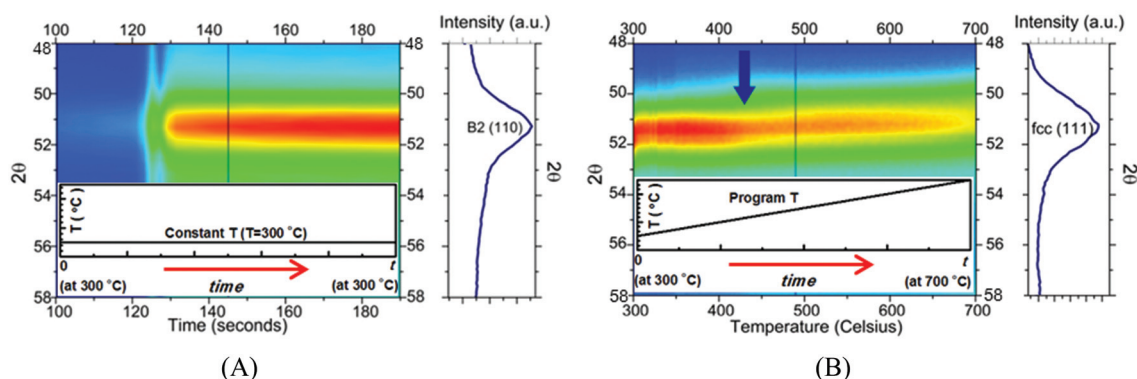

Fig. 2 Color map of the evolution of the intensity of peaks in the XRD patterns for a Pd : Cu NP mixture on a carbon-black substrate upon heating. (A) Isothermal heating at 300 °C under a He gas atmosphere. The evolution indicates the formation of the chemically ordered B2-type phase. (B) Heating from 300 °C to 700 °C under a H_2 atmosphere. The evolution indicates the transformation of the B2/bcc alloy phase into a chemically disordered fcc-type alloy phase. Insert panels illustrate the temperature run during XRD data collection. The vertical arrow in (B) indicates the starting point of the bcc-to-fcc phase transition.
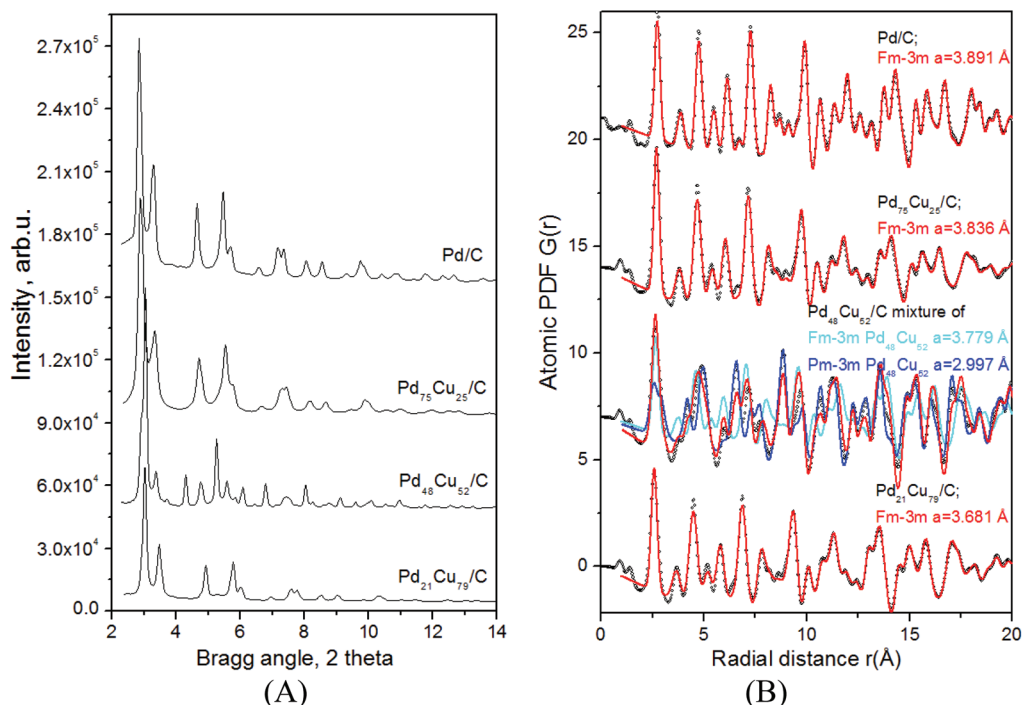
Fig. 3 Experimental HE-XRD patterns (A) for pure Pd and Pd–Cu alloy NPs. The patterns for $Pd_{75}Cu_{25}$ and $Pd_{25}Cu_{75}$ NPs are very similar to that for pure Pd NPs indicating that NPs are a single phase of the fcc-type structure. The HE-XRD pattern for $Pd_{48}Cu_{52}$ NPs shows extra peaks indicating the presence of an extra second phase. Experimental (symbols) and model (lines in red and blue) atomic PDFs (B) for pure Pd and Pd–Cu NPs. Model PDFs for pure Pd, $Pd_{75}Cu_{25}$ and $Pd_{21}Cu_{79}$ NPs are based on a model featuring a single nanophase with the fcc-type (space group (S.G.): $Fm\bar{3}m$) structure. NP lattice parameters based on the atomic PDF data are given by each data. Note, lattice parameters for bulk Pd and Cu are 3.891 Å and 3.615 Å, respectively. The experimental PDF for $Pd_{50}Cu_{50}$ NPs can be approximated by a model featuring two coexisting nanoalloy phases. Both phases are of the cubic type structure but differ in the degree of chemical ordering. One of the phases is completely chemically disordered and may be described in terms of a fcc-type (S.G. $Fm\bar{3}m$) structure. The other phase is completely chemically ordered and may be described in terms of a bcc-type (S.G. $Pm\bar{3}m$) type structure. The model fit lattice parameters of the two nanophases are given by the respective data set. For reference, the lattice parameter of bulk $Pd_{50}Cu_{50}$ (of space group $Pm\bar{3}m$) is 2.988 Å.

dominates in terms of abundance, as is the case with $Pd_{75}Cu_{25}$ and $Pd_{21}Cu_{79}$ NPs, the NPs appear as single phase nanoalloys of the fcc-type structure occurring with both bulk Pd and Cu. On the other hand, PdCu NPs wherein Pd and Cu species are almost equal in number appear to be segregated into chemically ordered bcc and chemically disordered fcc-type phases.

Both phases are known to occur in the bulk state.[33] In the chemically ordered alloy phase, Pd and Cu atoms occupy the vertices of two interpenetrating simple cubic lattices as shown in Fig. 4. As a result, each Cu atom has 8 Pd atoms as the first neighbors and a second coordination sphere rich in Cu atoms. Correspondingly, Pd atoms have 8 Cu atoms as the first neigh-
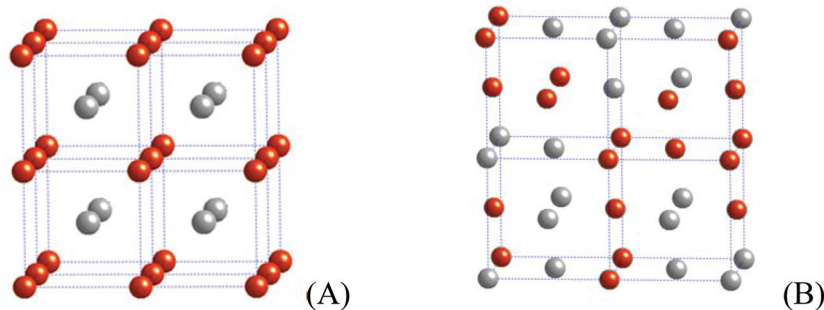

Fig. 4 (A) Fragment of the chemically ordered $Pd_{50}Cu_{50}$ ($Pm\bar{3}m$) cubic structure. The structure features alternating layers of Pd (gray) and Cu (red) atoms. (B) Fragment of the chemically disordered $Pd_{50}Cu_{50}$ ($Fm\bar{3}m$) cubic structure. It features a solid-solution of Pd and Cu atoms occupying the vertices of a face-centered cubic lattice.

bors and a second coordination sphere rich in Pd atoms. In the chemically disordered alloy, Pd and Cu atoms occupy the vertices of an fcc-type lattice at random. As a result, on average, each Pd and Cu species has virtually the same number of unlike first neighbors. Here it may be noted that the number of first atomic neighbors for NP surface atoms would be smaller than the numbers listed above because of the incomplete coordination spheres of these atoms. The fact that both chemically ordered and disordered Pd–Cu alloy nanophases appear very distinctly in the respective HE-XRD/ PDF data sets indicates that these phases comprise rather large atomic configurations. In other words, it indicates that Pd and Cu atoms in Pd–Cu alloy NPs interact, including forming large atomic configurations of very different chemical ordering patterns, and do not just mix together mechanistically. It may be conjectured that the relative abundance of these atomic configurations and the way they spread across NPs would be impacted by the post-synthesis thermochemical treatment and so PdCu NPs can be separated into the cluster-over-cluster and/or core–shell chemically ordered (bcc)/disordered (fcc) structural state.

Notably, a similar structural behavior was exhibited by (B-) PdCu alloy NPs treated under N_2 at 260 °C for 1 h and then under H_2 at 400 °C for 2 h. The behavior highlights the significant impact of post-synthesis thermochemical treatment on the atomic structure of PdCu alloy NPs, and the structure-dependent catalytic properties as discussed later.

(B) Structural evolution of nanoalloy catalysts during thermal treatment under an O_2 atmosphere by *in situ* HE-XRD/ PDF studies. Fresh $Pd_{21}Cu_{79}/C$ catalysts that are treated under

a N_2 atmosphere at 260 °C for 1 h, and then under a H_2 atmosphere at 400 °C for 2 h were probed with HE-XRD. In the measurement, the catalyst was further treated at 400 °C under 10 vol% O_2 for up to 30 min. The experimental HE-XRD patterns and the respective atomic PDFs are shown in Fig. 5. As shown in Fig. 5A, the fresh catalysts are single phase alloys with a very good degree of crystallinity (see the sharpness of the Bragg peaks in the respective HE-XRD pattern). The further heating treatment of the catalysts in O_2 does not improve their crystallinity further but induces a phase segregation manifested by the appearance of "extra" Bragg peaks when the heating temperature approaches 400 °C and lasts for about 30 min. Upon cooling back to room temperature, the "extra" Bragg peaks are intensified, *i.e.*, showing an increased degree of NP phase segregation.

To determine the structural evolution of fresh catalysts (B-) $Pd_{21}Cu_{79}/C$ NPs under the heating treatment, the experimental atomic PDFs of Fig. 5B were approached with a simple model based on an fcc-type structure. The model's "fcc-lattice" parameters were refined against the experimental PDFs and the results are summarized in Table S2.† As the data in Fig. 5B show, the first peak in the PDF for fresh $Pd_{21}Cu_{79}/C$ nanoalloy catalysts is symmetric and positioned at about 2.58 Å that is very close to the first neighbor Cu–Cu distance in bulk Cu (2.56 Å). For reference, the first neighbor Pd–Pd distance in bulk Pd is ~2.75 Å. Furthermore, the first peak, as well as all other peaks in the experimental PDFs, remains sharp until the NPs are heated up to 400 °C for about 30 min. Then the first PDF peak splits into two components positioned at 2.78 Å and 3.25 Å, respectively, indicating a nanophase segregation. The
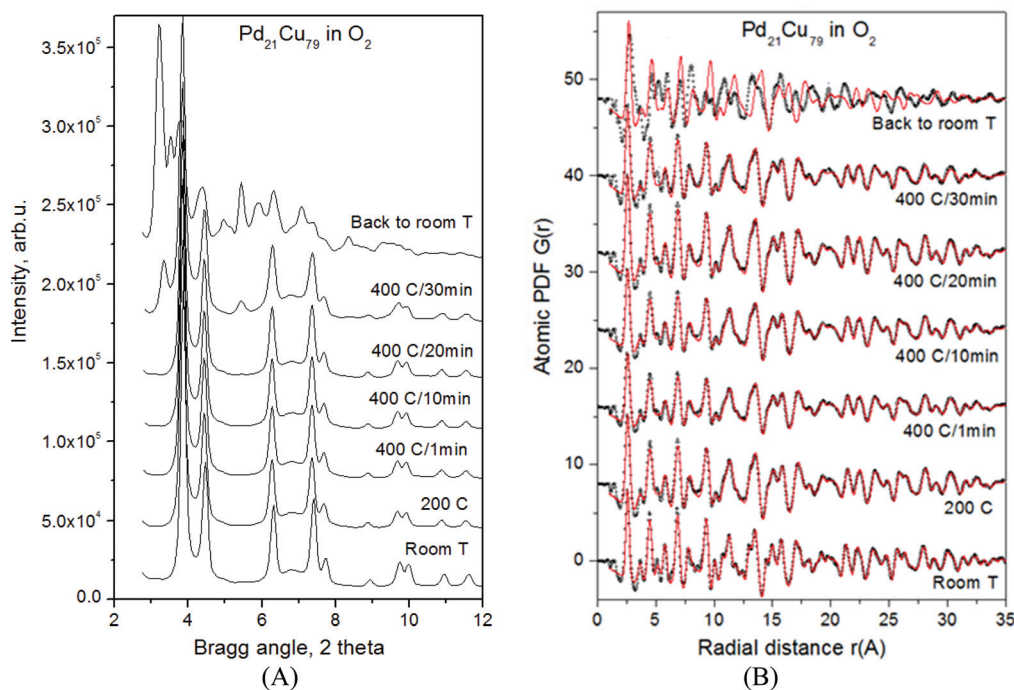

Fig. 5   (A) Experimental HE-XRD patterns for a sample of fresh $Pd_{21}Cu_{79}/C$ upon heating under O_2 up to 400 °C and (B) the respective experimental atomic PDFs (symbols) with the corresponding fitting curves (line in red).

results show that the thermochemical treatment of fresh nanoalloy catalysts can modify their atomic-scale structure further, including inducing nanophase segregation.

In summary, the phase state of fresh PdCu alloy NPs changes with the bimetallic composition. In particular, the Pd : Cu ratio of ~50 : 50 shows phase segregation whereas those with lower or higher Pd : Cu ratios exhibit a single phase. In addition, the phase state of fresh nanoalloys can be modified by further thermochemical treatment. The ability to change the phase state and so the atomic-scale structure by either changing the bimetallic composition and/or by subjecting the nanoalloys of a fixed bimetallic composition to further thermochemical treatment opens up new avenues to fine tuning the catalytic properties of nanoalloys. How the phase state, atomic structure and catalytic activity of the nanoalloy catalysts are correlated to each other is examined next.

3.4 Evaluation of the catalytic activity of Pd_nCu_{100-n} nanoalloy catalysts for CO oxidation

(A) Pd_nCu_{100-n}/C nanoalloys thermochemically treated under mild oxidative conditions. CO oxidation over Pd_nCu_{100-n}/C catalysts activated under relatively mild thermochemical treatment conditions, in particular under O_2/N_2 at 260 °C and then under H_2 at 400 °C, was examined. Note that the fresh catalysts were exposed to ambient air for an extensive period of time before evaluating their catalytic activities for CO oxidation. The results of the evaluation are summarized in Fig. 6 in terms of CO conversion (in %) and the temperature T_{50} at which a 50% conversion of CO to CO_2 is achieved. The data show a gradual increase in the NP catalytic activity with the increasing relative Pd content (Fig. 6B). A similar trend was observed when the catalytic evaluation was done after the fresh catalysts were further treated under an oxygen atmosphere at 260 °C (Fig. 6B(b)). The trend is consistent with the XPS determined evolution of Cu (2+, 1+) species with the composition of PdCu nanoalloys. In contrast to the catalytic activity

of Pd_nNi_{100-n} nanoalloys studied in our recent work,[38] Pd_nCu_{100-n} nanoalloys do not exhibit a minimum of T_{50} for $n \sim 50$. This may be attributed to the observed surface oxidation of Cu species in the PdCu nanoalloys and/or to the tendency of the nanoalloys to segregate into chemically ordered dominant and disordered nanophases at $n \sim 50$. This is further substantiated later by the differences of PdCu nanoalloy catalysts after treating under H_2 at 200 and 600 °C in terms of phase and surface oxidation states. Note that such a tendency was not observed with Pd_nNi_{100-n} nanoalloys,[38] which is understandable considering the differences in the alloy composition and structure. However, PdCu nanoalloys studied here appeared more durable as catalysts for CO oxidation as compared to pure Pt and Pt-based nanoalloys[41,42] since the latter have been found to exhibit a strong propensity of poisoning. In addition to the above tests, the $Pd_{54}Cu_{46}$ nanoalloy catalysts were also examined at 135 °C for at least 48 h, or even longer, which showed little deactivation at around 50% CO conversion.

The T_{50} value of PdCu nanoalloy catalysts for CO oxidation reaction was also evaluated after further thermochemical treatments, including (1) heating under H_2 at 200 °C for 30 min and (2) heating under H_2 at 600 °C for 30 min. The results are shown in Fig. 7A. Analysis of the results shows that (i) the nanoalloy catalysts after further treatment at 200 °C exhibit a higher activity than those treated at 600 °C; and (ii) the catalysts with a Pd : Cu ratio of 50 : 50 exhibit a maximal activity in comparison with those with a higher or lower Pd : Cu ratio. Furthermore, when the Pd : Cu ratio is smaller than 50 : 50, *i.e.*, the nanoalloy rich in Cu, the difference in T_{50} for nanoalloys treated under H_2 at 200 °C and 600 °C is small (only about 4 °C). On the other hand, for a Pd : Cu ratio higher than 50 : 50, as is the case with those with $n = 54$ and 75, the difference of T_{50} for nanoalloys treated under H_2 at 200 °C and 600 °C is relatively large (about 40 °C). A further examination of T_{10} values, at which a 10% conversion of CO is achieved (*i.e.*, "light-off temperature"), for the different thermal treat-
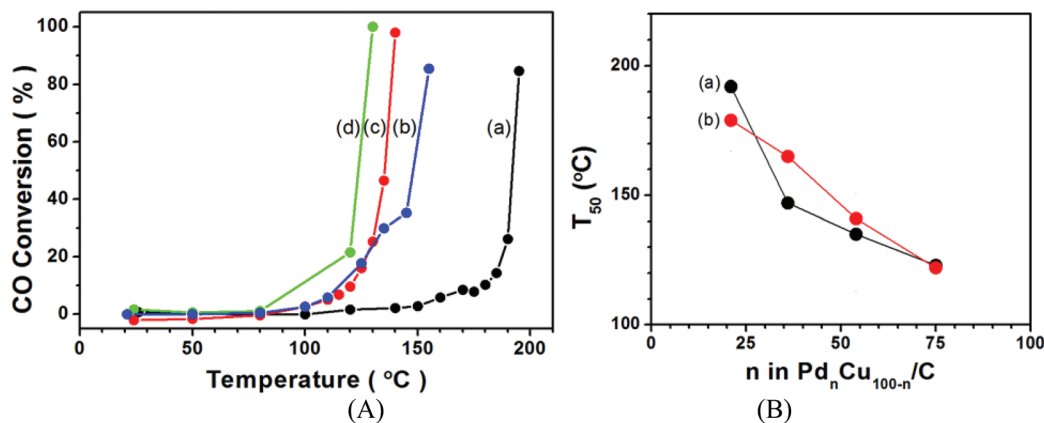

Fig. 6 (A) CO conversion (in %) over fresh Pd_nCu_{100-n}/C catalysts (n = 21 (a, black), 36 (b, blue), 54 (c, red), and 75 (d, green)); (B) T_{50} values *vs.* bimetallic composition for the fresh Pd_nCu_{100-n}/C catalysts (a, black) and the same catalysts after further treatment under O_2 at 260 °C for 30 min (b, red).
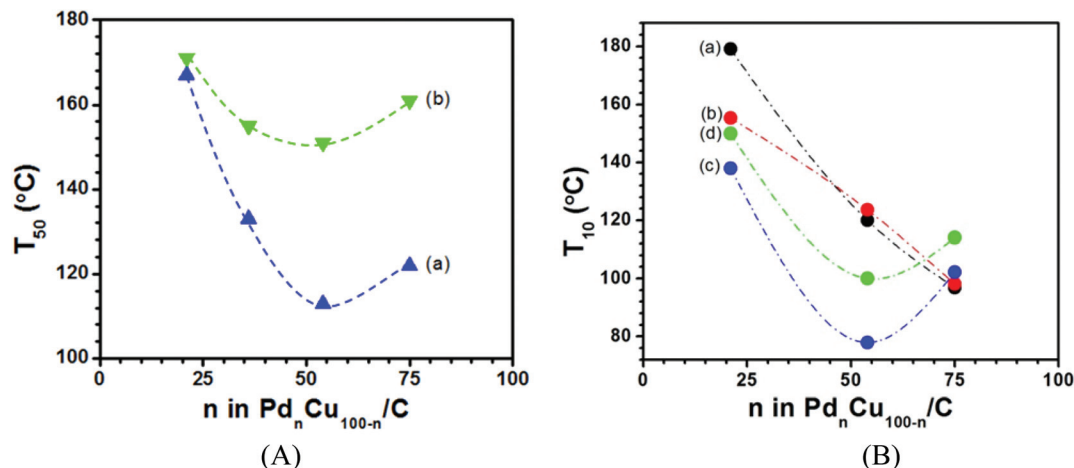
Fig. 7 (A) T_{50} values *vs.* bimetallic composition for Pd$_n$Cu$_{100-n}$/C nanoalloy catalysts treated under H$_2$ at 200 °C (a, blue) and at 600 °C (b, green); (B) T_{10} values *vs.* bimetallic composition for PdCu/C catalysts under the following conditions: (a) fresh (black); (b) further treated under O$_2$ at 260 °C for 30 min (red); (c) treated under H$_2$ at 200 °C for 30 min (blue) and (d) treated under H$_2$ at 600 °C for 30 min (green).

ment conditions (Fig. 7B) revealed a similar linear relationship of activity *vs.* composition for the fresh and oxidized catalysts, and a maximum of activity at 50 : 50 ratio for the reduced catalysts. It is believed that a phase transition of the type observed during heating a physical mixture of Pd and Cu nanoparticles (see Fig. 2) was operative under the oxidative and reductive treatment conditions. However, the phase structure observed for the reduced nanoalloy catalysts did not follow the trend observed for mixing of Pd and Cu nanoparticles, indicating the importance of the atmosphere and atomic structure to the phase properties. Moreover, the phase-segregated state for the fresh Pd$_{54}$Cu$_{46}$/C catalysts was found to remain to a certain degree upon H$_2$ treatment at 200 °C, as supported by PDF analysis (see Fig. S3†). The chemically disordered fcc structure fits better for catalysts treated under H$_2$ at 200 °C, indicating that the enrichment of the fcc phase may be responsible for the enhanced activity. To further substantiate this assessment, we measured the relative surface composition of Pd on the PdCu catalysts using an electrochemical method, *e.g.*, determining the electrochemically active surface area (ECA) characteristic of Pd by cyclic voltammetry (see Table S3†). With fresh catalysts, the ECA value was shown to increase with Pd%, exhibiting a maximum at an ~50 : 50 ratio of Pd : Cu. This trend appears to be inconsistent with the catalytic data for fresh catalysts, though there seems to be some consistency with the hydrogen-reduced catalysts, indicating that the surface Pd composition is not necessarily the sole determining factor for the observed composition dependence of the catalytic activity. There is a need for future studies to establish a comprehensive correlation among the composition, atomic structure, phase state, and catalytic activity. This assessment will be further supported in a later section through examining the PdCu catalysts synthesized by another method which produced the catalysts predominated by the fcc phase structure.

(B) Pd$_n$Cu$_{100-n}$/C catalysts thermochemically treated under deep oxidative conditions. CO oxidation over Pd$_n$Cu$_{100-n}$/C nanoalloy catalysts was also studied on NPs treated under O$_2$ at 450 °C for 30 min and then under H$_2$ at 300 °C for 30 min. The results (Fig. S4†) show that the catalytic activity of the nanoalloy catalysts is largely recovered after H$_2$ treatment at 300 °C for 30 min. This is an unusual outcome considering that a significant fraction of NPs coalesces severely under O$_2$ treatment as indicated by *in situ* HE-XRD/PDF experiments and thermogravimetric analysis (see Fig. 5 and S5†). Both reduced and oxidized Pd$_n$Cu$_{100-n}$/C catalysts with $n \sim$ 50 : 50 show an activity similar to that of monometallic Pd/C catalysts (Fig. S4†). Also, the T_{50} values for different batches of Pd$_n$Cu$_{100-n}$ catalysts with $n \sim$ 50 differ by 30 °C, which likely reflects the different exposure of the respective batches to the ambient atmosphere. The largely identical T_{50} values for the nanoalloy catalysts treated under a H$_2$ atmosphere support this conclusion. In contrast to the case of the nanoalloy catalysts treated under mild oxidation conditions (*i.e.*, 260 °C), no minimum in T_{50} values is observed when the same catalysts are treated under deep oxidation conditions (*i.e.*, 450 °C).

(C) Pd$_n$Cu$_{100-n}$ nanoalloys deposited on different supports. CO oxidation was also studied for Pd$_{48}$Cu$_{52}$ nanoalloys deposited on different supports. The results for the nanoalloys treated under a H$_2$ atmosphere at 300 °C for 30 min are summarized in Fig. S6A.† The results indicate that the catalytic activity is highest with PdCu nanoalloys supported on TiO$_2$ and diminishes in the order of TiO$_2$ > CeO$_2$ > SiO$_2$ > C. The values of T_{50} for nanoalloys deposited on different supports and then subjected to an oxidative (under O$_2$ at 450 °C for 30 min) or reductive (under H$_2$ at 300 °C for 30 min) treatment are shown in Fig. S6B.† It shows that the reduced nanoalloys have a higher activity than the oxidized ones. Also, "active" supports such as TiO$_2$ and CeO$_2$ promote the oxidation of CO over PdCu nanoalloys since T_{50} drops by 20–100 °C in compari-

son with the case when "inert" supports such as SiO_2 and carbon are used. The PdCu nanoalloys supported on carbon exhibit the lowest activity among all oxidized catalysts, which is partly due to "carbon support burning" effects during the thermochemical treatment (see Fig. S5†).

(D) Pd_nCu_{100-n} catalysts synthesized by a different method. PdCu catalysts prepared by a different synthesis method were also examined to assess the above findings. One example involved Pd_nCu_{100-n} catalysts synthesized using ethylene glycol as the solvent ((E-) PdCu, see the Experimental section). The (E-) PdCu/C catalysts were shown to exhibit a single cubic, mostly fcc-type phase. A gradual shift in the position of the (111) Bragg peak toward higher diffraction angles was observed with increasing Cu in the NPs. The shift indicates that the fcc-type structure of (E-) PdCu/C NPs does not undergo abrupt changes with the bimetallic composition. The results of the XRD experiments were largely confirmed by atomic PDF analysis. As shown in Fig. S3C,† the experimental atomic PDFs for (E-) Pd–Cu alloy NPs can be well approximated with a structure model featuring a chemically random alloy with a fcc-type structure.

The catalysts of the (E-) Pd–Cu/C nanoalloys were activated by the same thermochemical treatment used for the (B-) Pd–Cu nanoalloys, *i.e.*, the nanoalloys were first heated at 260 °C under O_2 for 30 min and then heated either at 200 °C or 600 °C under H_2 for another 30 min. A representative set of the CO conversion and T_{10} values is given in Fig. 8.

The results reveal that (B-) PdCu and (E-) PdCu nanoalloys exhibit somewhat different catalytic properties. In particular, a maximum of catalytic activity was revealed for (E-) PdCu/C catalysts at Pd : Cu ~ 50 : 50 ratio, independent of the treatment conditions (Fig. 8B). To understand the results, both (B-) PdCu/C and (E-) PdCu/C treated under H_2 at 200 °C were examined by PDF analysis (Fig. S3†). In comparison with fresh catalysts treated under O_2 at 260 °C and then under H_2 at 400 °C followed by exposure to air before testing, the (B-) PdCu/C cata-

lysts treated under H_2 at 200 °C were found to remain in the phase-segregated state with the co-existing chemically ordered and disordered phases. A similar fcc like chemically disordered phase structure was revealed for the (E-) PdCu/C catalysts treated at 200 °C. This result indicates that there is a significant correlation between the catalytic activity and the phase state, which is influenced not only by synthesis and treatment conditions but also by particle size. There is a 30 °C drop in the T_{10} value from (B-) PdCu to (E-) PdCu at Pd : Cu ~ 50 : 50 ratio, which is largely attributed to the predominated fcc structure in (E-) catalysts (see Fig. S3†). This is also evidenced by data from thermal treatment under a H_2 atmosphere at 200 °C, at which the T_{10} value could largely correlate with a better fit by the fcc type structure for (B-) $Pd_{54}Cu_{46}/C$ under H_2 at 200 °C although the particle size effect also needs to be considered. Regardless of the size difference, there is a clear increase in the fcc-component's lattice parameters from 400 to 200 °C treatments, *i.e.*, 3.779 to 3.807 Å for (B-) $Pd_{54}Cu_{46}$, and 3.791 to 3.832 Å for (E-) $Pd_{58}Cu_{42}/C$. This change is consistent with the expansion of interatomic distances, which has been observed recently for $Pd_{50}Ni_{50}$ catalysts in activity enhancement.[38] However, for PdCu nanoalloys, the coexistence of chemically ordered and disordered phases posed a complication to the computational modeling at this time, which is a part of our on-going work. This finding is further assessed by examining the ECA data on the surface area of Pd for (E-) PdCu catalysts (see Table S3†). While the ECA values are indeed higher than those for (B-) PdCu catalysts at similar compositions, which is consistent with the smaller particle size of (E-) PdCu NPs, they showed a gradual increase with Pd% for (E-) PdCu catalysts without exhibiting a maximum. This finding suggests again that the surface area of Pd was not the key factor for the enhanced activities at ~50 : 50 ratio. Note that the increase in activity from 400 to 200 °C treatments is greater for (B-) $Pd_{54}Cu_{46}$ (T_{50} from 135.3 to 112.7 °C) than that for (E-) $Pd_{58}Cu_{42}/C$ (T_{50} from 121.3 to
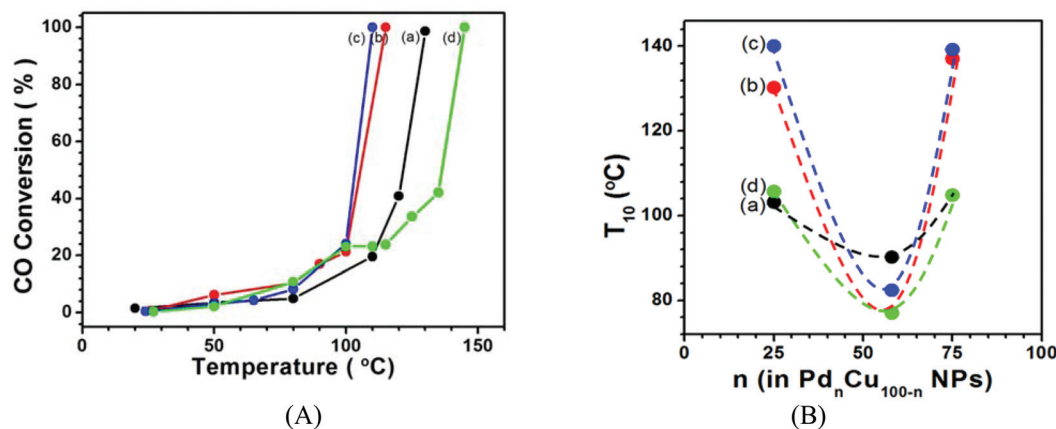

Fig. 8 (A) CO conversion (in %) over $Pd_{58}Cu_{42}/C$ catalysts treated: (1) fresh (a, black); (2) under an oxygen atmosphere at 260 °C for 30 min (b, red) and then (3) under a hydrogen atmosphere at 200 °C for 30 min (c, blue) or (4) under a hydrogen atmosphere at 600 °C for 30 min (d, green). (B) T_{10} values as a function of bimetallic composition for (E-) PdCu/C.
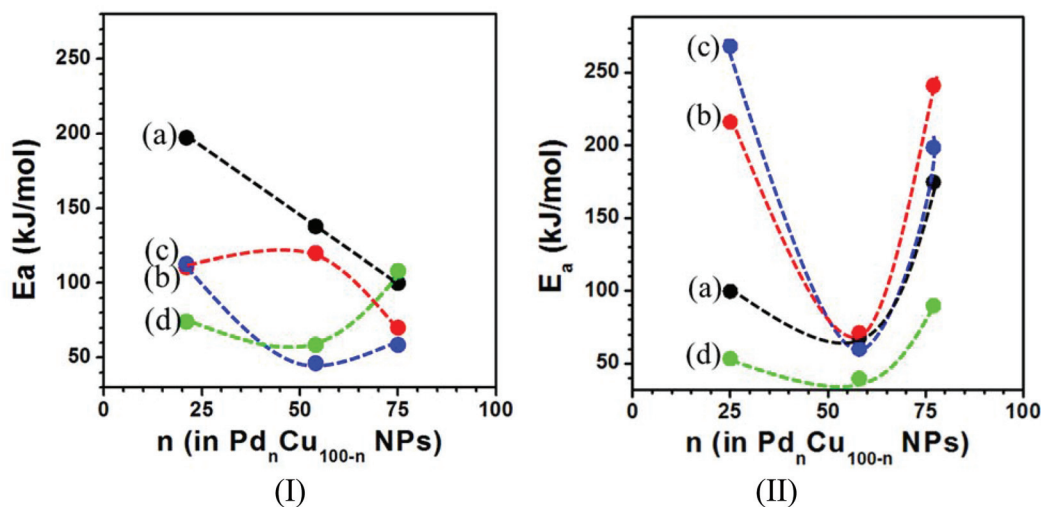
Fig. 9 Activation energy *vs.* Pd% (*n*) for two sets of Pd_nCu_{100-n}/C nanoalloy catalysts ((B-) PdCu(I) and (E-) PdCu(II)). Both catalysts were examined under the following treatment conditions: (a) fresh (black curve); (b) treated under O_2 at 260 °C (red curve); (c) under H_2 at 200 °C (blue curve) and (d) under H_2 at 600 °C (green curve). Data are derived from the Arrhenius plots for CO oxidation.

103.2 °C), indicative of the role of the phase change from fcc + bcc to fcc in influencing the activity.

To further substantiate the catalytic activity in terms of bi-metallic composition, the kinetics of CO oxidation were analyzed based on the above experimental data (see Fig. S7 and Table S3†). The activation energy for CO oxidation (E_a) derived from the dependence of CO conversion or the reaction rate *vs.* $1/T$ is clearly dependent on the bimetallic composition (Fig. 9). For both (B-) PdCu and (E-) PdCu catalysts, the trend of the activation energy as a function of composition is in good agreement with the trend for T_{10} or T_{50} values. Interestingly, both (B-) and (E-) PdCu showed a similar activation energy around 40–60 kJ mol^{-1} at an ~50:50 ratio of Pd:Cu for the catalysts treated under H_2 at either 200 or 600 °C, whereas their T_{50} or T_{10} values displayed a difference of 50 °C. This phenomenon at 200 °C was accompanied by the expansion of lattice parameters.

(E) Structural modeling and theoretical consideration. It is evident that the structural and catalytic properties are strongly dependent on a combination of the bimetallic composition and the phase structure. On the basis of the structure model of bcc and fcc phases (Fig. 4), the Pd and Cu atoms on different facets are clearly more intermixed in the fcc phase than in the bcc phase (Fig. 10). This type of ensemble effect in terms of composition, or atomic coordination structure, and the atomic arrangement in different phases as a result of Pd and Cu mixing patterns are partially responsible for the enhanced catalytic activity for the catalysts with the fcc-phase at a Pd:Cu ratio of 50:50.

The enhanced activity of the catalyst at a Pd:Cu ratio of 50:50 is further assessed based on density functional theory (DFT) calculation with a small cluster model featuring an optimal tetrahedral structure for CO adsorption (Fig. S8 and Table S4†) in which CO is adsorbed on the Pd atom for
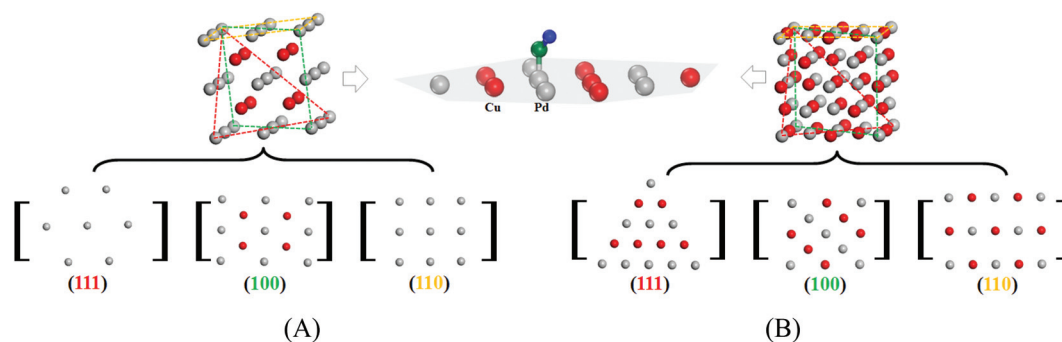

Fig. 10 Illustrations of the degree of intermixing of Pd (grey) and Cu (red) atoms on different facets based on structure models for bcc (A) and fcc (B) phases. Insert: illustration of CO (*e.g.*, C atom (green) and O (blue)) adsorption on the (111) facet of the fcc phases.

Pd$_x$Cu$_{4-x}$ clusters (x = 1, 2, 3, 4). The preliminary results reveal the most negative value for the adsorption energy and most upshift for the d-band center for x = 2. Also, the C–O bond length is the longest and the Pd–C bond is the shortest for x = 2. These findings are consistent with other studies in terms of the correlation between the d-band center shift and CO adsorption energy.[46] For example, the DFT study of PdCu(111) alloy slab models indicated a strong correlation between the CO adsorption energy and the d band center in which a 1-to-1 Pd : Cu alloy ratio exhibits a greater adsorption energy and upshift of the d band center in comparison with the 3-to-1 Pd : Cu alloy ratio,[27] in agreement with the results of our DFT study. In the case of Pd-rich PdCu (111) alloy models, DFT calculation showed that CO is significantly destabilized in the multifold sites relative to the atop site.[29] For DFT calculation of the small clusters, though further refinements of the cluster size and geometry are needed, there is a qualitative indication that the ensemble effect plays an important role in the enhanced catalytic activity for CO oxidation over the PdCu catalyst with a Pd : Cu ∼ 50 : 50 ratio. We are working on refined models considering nanoparticle facet and support effects, which will be described in a future report.

4. Conclusion

Altogether, the results show that the catalytic activity of PdCu nanoalloys strongly depends on the synthesis conditions, bimetallic composition, and the post-synthesis thermochemical treatment conditions, including temperature, duration and gas environment. A catalytic synergy of Pd and Cu species in nanoalloys with a Pd : Cu ratio close to 50 : 50 is operative in leading to an enhanced catalytic performance for CO oxidation reaction. The structural characterization shows that Pd and Cu species in such nanoalloy catalysts are predominantly randomly mixed with respect to each other forming an fcc-like structure. If the nanoalloys form a chemically ordered bcc-type structure or segregate into fcc- and bcc-type phases, the catalytic activity for CO oxidation could be reduced depending on the detailed interatomic distance and ordering. In these subtle atomic structure ordering–disordering processes triggered by changes in the bimetallic composition and/or synthesis and treatment conditions of nanoalloys, it is the optimal ordering of the nearby Pd and Cu atoms with respect to each other, *i.e.* the so-called atomic ensemble effect along with elongated interatomic distances, that contribute most to the enhanced catalytic activity of PdCu nanoalloys at a Pd : Cu ratio close to 50 : 50. Therefore, efforts aimed at improving the catalytic activity of PdCu nanoalloys by refining the atomic sites active for CO oxidation should, among others, concentrate on minimizing the degree of phase segregation and/or chemical ordering in PdCu nanoalloys with a 50 : 50 bimetallic ratio. Implications of these findings to rationalizing the preparation of Pd-based nanoalloy catalysts by design are very significant, which is reflected in part of our on-going investigations.

References

1 H. Zhang, M. S. Jin and Y. N. Xia, *Chem. Soc. Rev.*, 2012, **41**, 8035–8049.
2 H. J. Zhang, T. Watanabe, M. Okumura, M. Haruta and N. Toshima, *Nat. Mater.*, 2012, **11**, 49–52.
3 G. J. Hutchings, *Dalton Trans.*, 2008, 5523–5536.
4 M. S. Chen, D. Kumar, C. W. Yi and D. W. Goodman, *Science*, 2005, **310**, 291–293.
5 F. Gao and D. W. Goodman, *Chem. Soc. Rev.*, 2012, **41**, 8009–8020.
6 G. J. Hutchings and C. J. Kiely, *Acc. Chem. Res.*, 2013, **46**, 1759–1772.
7 M. H. Shao, K. Sasaki and R. R. Adzic, *J. Am. Chem. Soc.*, 2006, **128**, 3526–3527.
8 M. H. Shao, K. Shoemaker, A. Peles, K. Kaneko and L. Protsailo, *J. Am. Chem. Soc.*, 2010, **132**, 9253–9255.
9 D. I. Enache, J. K. Edwards, P. Landon, B. Solsona-Espriu, A. F; Carley, A. A. Herzing, M. Watanabe, C. J. Kiely, D. W. Knight and G. J. Hutchings, *Science*, 2006, **311**, 362–365.
10 L. Kesavan, R. Tiruvalam, M. H. Ab Rahim, M. I. bin Saiman, D. I. Enache, R. L. Jenkins, N. Dimitratos, J. A. Lopez-Sanchez, S. H. Taylor, D. W. Knight, C. J. Kiely and G. J. Hutchings, *Science*, 2011, **331**, 195–199.
11 E. Antolini, *J. Power Sources*, 2007, **170**, 1–12.
12 M. Cargnello, J. J. Delgado Jaen, J. C. Hernandez Garrido, K. Bakhmutsky, T. Montini, J. J. Calvino Gamez, R. J. Gorte and P. Fornasiero, *Science*, 2012, **337**, 713–717.
13 P. Paalanen, B. M. Weckhuysen and M. Sankar, *Catal. Sci. Technol.*, 2013, **3**, 2869–2880.
14 T. Ward, L. Delannoy, R. Hahn, S. Kendell, C. J. Pursell, C. Louis and B. D. Chandler, *ACS Catal.*, 2013, **3**, 2644–2653.
15 J. Greeley, I. E. Stephens, A. S. Bondarenko, T. P. Johansson, H. A. Hansen, T. F. Jaramillo, J. Rossmeisl, I. Chorkendorff and J. K. Norskov, *Nat. Chem.*, 2009, **1**, 552–556.
16 C. C. Jin, X. J. Sun, Z. D. Chen and R. L. Dong, *Mater. Chem. Phys.*, 2012, **135**, 433–437.
17 C. X. Xu, A. H. Liu, H. J. Qiu and Y. Q. Liu, *Electrochem. Commun.*, 2011, **13**, 766–769.
18 Z. Yin, W. Zhou, Y. J. Gao, D. Ma, C. J. Kiely and X. H. Bao, *Chem. – Eur. J.*, 2012, **18**, 4887–4893.
19 F. Gobal and R. Arab, *J. Electroanal. Chem.*, 2010, **647**, 66–73.
20 F. Fouda-Onana, S. Bah and O. Savadogo, *J. Electroanal. Chem.*, 2009, **636**, 1–2.

21 J. Yin, S. Shan, M. S. Ng, L. F. Yang, D. Mott, W. Fang, N. Kang, J. Luo and C. J. Zhong, *Langmuir*, 2013, **29**, 9249–9258.

22 S. Y. Shen, T. S. Zhao, J. B. Xu and Y. S. Li, *J. Power Sources*, 2010, **195**, 1001–1006.

23 K. Persson, A. Ersson, K. Jansson, N. Iverlund and S. Jaras, *J. Catal.*, 2005, **231**, 139–150.

24 B. C. Kanra, J. C. Bertolini and J. L. Rousset, *J. Mol. Catal. A: Chem.*, 1998, **129**, 233–240.

25 W. J. Tang, L. Zhang and G. Henkelman, *J. Phys. Chem. Lett.*, 2011, **2**, 1328–1331.

26 Y. G. Chen, L. Zhuang and J. T. Lu, *Chin. Chem. Lett.*, 2007, **18**, 1301–1304.

27 N. Lopez and J. K. Norskov, *Surf. Sci.*, 2001, **477**, 59–75.

28 Y. Sha, T. H. Yu, B. V. Merinov and W. A. Goddard, *ACS Catal.*, 2014, **4**, 1189–1197.

29 E. Jeroro, M. P. Hyman and J. M. Vohs, *Phys. Chem. Chem. Phys.*, 2009, **11**, 10457–10465.

30 M. Fernandez-Garcia, A. Martinez-Arias, C. Belver, J. A. Anderson, J. C. Conesa and J. Soria, *J. Catal.*, 2000, **190**, 387–395.

31 J. Lobodacackovic, A. Hammoudeh, M. S. Mousa and J. H. Block, *Vacuum*, 1995, **46**, 411–415.

32 F. G. Wang, H. J. Zhang and D. N. He, *Environ. Technol.*, 2014, **35**, 347–354.

33 M. H. Martin, J. Galipaud, A. Tranchot, L. Roue and D. Guay, *Electrochim. Acta*, 2013, **90**, 615–622.

34 F. C. Zhu, G. S. Ma, Z. C. Bai, R. Q. Hang, B. Tang, Z. H. Zhang and X. G. Wang, *J. Power Sources*, 2013, **242**, 610–620.

35 C. G. Hu, H. H. Cheng, Y. Zhao, Y. Hu, Y. Liu, L. M. Dai and L. T. Qu, *Adv. Mater.*, 2012, **24**, 5493–5498.

36 S. Y. Shan, J. Luo, L. F. Yang and C. J. Zhong, *Catal. Sci. Technol.*, 2014, **4**, 3570–3588.

37 S. Y. Shan, J. Luo, J. F. Wu, N. Kang, W. Zhao, H. Cronk, Y. G. Zhao, P. Joseph, V. Petkov and C. J. Zhong, *RSC Adv.*, 2014, **4**, 42654–42669.

38 S. Y. Shan, V. Petkov, L. F. Yang, J. Luo, P. Joseph, D. Mayzel, B. Prasai, L. Y. Wang, M. Engelhard and C. J. Zhong, *J. Am. Chem. Soc.*, 2014, **136**, 7140–7151.

39 V. Petkov, B. Prasai, Y. Ren, S. Shan, J. Luo, P. Joseph and C. J. Zhong, *Nanoscale*, 2014, **6**, 10048–10061.

40 V. Mukundan, J. Yin, P. Joseph, J. Luo, S. Y. Shan, D. N. Zakharov, C. J. Zhong and O. Malis, *Sci. Technol. Adv. Mater.*, 2014, **15**, 025002.

41 L. Yang, S. Shan, R. Loukrakpam, V. Petkov, Y. Ren, B. N. Wanjala, M. H. Engelhard, J. Luo, J. Yin, Y. Chen and C. J. Zhong, *J. Am. Chem. Soc.*, 2012, **134**, 15048–15060.

42 S. Y. Shan, V. Petkov, L. F. Yang, D. Mott, B. N. Wanjala, F. Cai, B. H. Chen, J. Luo and C. J. Zhong, *ACS Catal.*, 2013, **3**, 3075–3085.

43 V. Petkov, S. Shan, P. Chupas, J. Yin, L. F. Yang, J. Luo and C. J. Zhong, *Nanoscale*, 2013, **5**, 7379–7387.

44 S. M. Oxford, P. L. Lee, P. J. Chupas, K. W. Chapman, M. C. Kung and H. H. Kung, *J. Phys. Chem. C*, 2010, **114**, 17085–17091.

45 T. Egami and S. J. L. Billinge, *Underneath the Braggs' Peak*, Pergamon, Amsterdam, Netherlands, 2003.

46 S. Sakong, C. Mosch and A. Gross, *Phys. Chem. Chem. Phys.*, 2007, **9**, 2216–2225.